PERGAMON

International Journal of Heat and Mass Transfer 41 (1998) 4151–4166

International Journal of HEAT and MASS TRANSFER

Heat transfer enhancement of a finned oval tube with punched longitudinal vortex generators in-line

Y. Chen, M. Fiebig, N. K. Mitra*

Institut für Thermo- und Fluiddynamik, Ruhr-Universität Bochum, D-44780 Bochum, Germany

Received 15 October 1997; in final form 24 March 1998

Abstract

To explore the interaction of the vortical flow generated by punched delta-winglet pairs (DWPs) with in-line arrangement and to explore their influence on the heat transfer enhancement (HTE) and on flow loss penalty (FLP) in a high performance finned oval tube (FOT) heat exchanger element, three-dimensional flow and conjugate heat transfer in an FOT were calculated for a thermally and hydrodynamically developing laminar flow ($Re = 300$) by solving the Navier–Stokes and energy equations with a Finite-Volume Method in body-fitted grids. The conjugate heat transfer was realized by iterations of the energy equation in the flow field and the conduction equation in the fin. FOT with one to three in-line DWPs ($\beta = 30^\circ$, $\Lambda = 2$, $h = H$) were investigated. Velocity and temperature fields, vortex formation, local heat transfer distributions and global results were presented. The LVs of the incoming flow intensified the LVs downstream of the second and the third winglet. For $Re = 300$ and $Fi = 500$, the ratios of HTE to FLP $(j/j_0)/(f/f_0)$ were 1.04, 1.01 and 0.97 for an FOT with one, two and three DWPs in-line respectively.

Nomenclature

a thermal diffusivity, coefficient
A area
b span
B width
h convective heat transfer coeff.; height of the winglet
H channel height
J Jacobian
k thermal conductivity
L length
p pressure
R_{Nu} Nusselt number enhancement
R_P thermohydraulic performance factor
t time
T temperature
u, v, w velocity components
x, y, z Cartesian co-ordinates.

Greek symbols

ϕ general variable
β cofactor, angle of attack
Λ aspect ratio
ξ, η, ζ generalized co-ordinates
δ fin thickness
ν kinematic viscosity
ρ density.

Subscripts and superscripts

0 reference value
B bulk
cs cross-sectional averaged
f fin
frt frontal
ht heat transfer
i, j, k index
m mean value
sp span averaged
T tube
VG vortex generator
z $z = 0$ or $z = 1$
* dimensional (superscript).

Dimensionless parameter and variables

$Bi = h^*\delta^*/k_f^*$ Biot number

* Corresponding author. Tel.: 00 49 234 700 6444; Fax: 0049 234 7094 162; E-mail: Mitra@VTP.ruhr-uni-bochum.de

0017–9310/98 $19.00
PII: S0017–9310(98)00130–6

$$f = \frac{\Delta p^*}{\rho^* u_0^{*2}/2}\frac{A_{\mathrm{frt}}^*}{A_{\mathrm{ht}}^*}$$ friction factor

$$Fi = \frac{k_{\mathrm{f}}^*}{k^*}\frac{\delta^*}{H^*}$$ fin parameter 1

$$Ft = \frac{a_{\mathrm{f}}^*}{a_0^*}\frac{1}{Pe}$$ fin parameter 2

$$j = \frac{Nu_{\mathrm{m}}}{RePr^{1/3}}$$ Colburn j factor

$$Nu = \frac{h^*H^*}{k_0^*} = \frac{\dot{q}_{z0}}{(T_{\mathrm{f}} - T_{\mathrm{B}})}$$ Nusselt number

$$Pe = Re\ Pr$$ Peclet number

$$Pr = v_0^*/a_0^*$$ Prandtl number

$$\dot{q} = \left.\frac{\partial T}{\partial z}\right|_{z=0} - \left.\frac{\partial T}{\partial z}\right|_{z=1}$$ fin heat flux

$$Re = \frac{u_0^* H^*}{v_0^*}$$ Reynolds number.

1. Introduction

To reduce the thermal resistance on the gas side of a gas–liquid heat exchanger, fins are applied, as in the case of a finned tube heat exchanger shown in Fig. 1. To improve the performance of the fins, heat transfer enhancement (HTE) on the fins is necessary. Mechanisms for passive HTE are: developing-boundary layers, swirl and flow destabilization. Wing-type longitudinal vortex generators (WVG) as those sketched in Fig. 2 can generate all three mechanisms for the passive HTE [1–3].

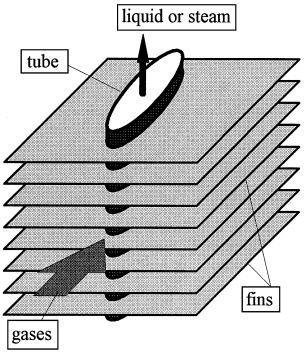

Fig. 1. Element of a finned tube heat exchanger core.

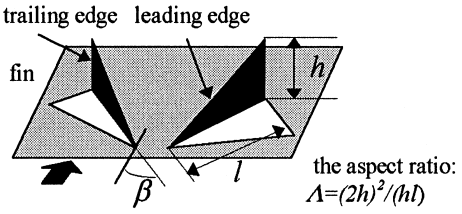

Fig. 2. Schematic of a DWP.

In the earlier studies [4–5], flow and heat transfer in an FOT with a punched DWP near the entrance were investigated. Longitudinal vortices (LVs) generated by the winglet last to the exit. Winglets with angle of attack $\beta = 30^\circ$ and aspect ratio $\Lambda = 2$ provide the best thermohydraulic performance. The spanwise averaged Nusselt number enhancement increased abruptly at the beginning of the winglet. It falls down steeply behind the winglet and remains farther downstream at a relatively low level. Further enhancement with winglets downstream is necessary. Experimental investigations with two rows of delta winglet pairs (DWPs) by Tiggelbeck [6] reveal that the second DWP acts as a booster for the coming LVs, if the winglets are in-line. The outer region of the LVs is more unsteady in the wake of the second DWP than that of the first DWP. The critical angle of attack, over which a transition from LV-dominated to transverse vortices dominated wake flow occurs, is reduced from 75° for the first row DWP to 65° for the second row. The best distance between the first and the second row is 7 H. Numerical investigation by Güntermann [7] with periodically LVG-rows revealed that the repeated disturbance from upstream resulted in a self-oscillation of the flow. Bastani [8] and Valencia [9] investigated the heat transfer in two and three rows of finned tube element with two and three DWP-rows. Bastani studied the finned circular tube in laminar flow, while Valencia compared the finned circular and flat tube in both laminar and turbulent flows. The Nusselt number enhancement by the winglet increases with increasing winglet rows. For high Reynolds number ($Re = 2670$ [9]), even the absolute local Nu values downstream are higher than that upstream. This is not observed in the low Reynolds number region [8].

The LVs behind the second winglet row are found to be stronger and more unsteady than the first row [6]. But how do the on-coming LVs strengthen the 'newly' generated LVs? Does the coming LV-core overlap the 'new' LV-core? No report is available. This paper addresses these questions. The other purpose of this paper is to compare the thermohydraulic performance of FOTs with one to three rows of winglets.

2. Theoretical formulation and solution procedure

2.1. Geometrical model

Figure 3(a) shows an FOT element with a punched DWP. Two fins with thickness d form a channel of height H, width B ($= 9.1H$) and length L ($= 15.4H$). An oval tube ($L_T/B_T = 5.5$, cross sectional area $A_{T,CS} = 24.6H^2$) is located at the center of the fin. The ratio of fin to tube area is 8.44. Such geometry is commonly used in industry [10]. Winglets are punched out of the fin. The thickness of the winglet is assumed to be zero and the height of the winglet (h) is equal to the channel height (H) so that the DWP can also function as a pitch holder of the fin. The angle of attack β of the winglet is equal to 30° and the aspect ratio Λ is equal to 2. For small Reynolds numbers, the flow is steady and the computational domain can be reduced by using symmetry conditions on the mid-plane of the channel ($y = B/2$). The domain is extended by 6 H over the exit to ensure a recirculation-free flow there. Figure 3(b) shows the computational domain and the employed boundary conditions. In this paper, the performance of four configurations with one to three in-line winglets (Fig. 3(c), Table 1) is compared. There is no winglet in configuration 0, one punched winglet in configuration 3. There are two winglets in configurations 6 and 7, and three winglets in configuration 11. The position of the first winglet is the same in all configurations. In configuration 6, the second winglet is located at 1/3 of the distance from the first winglet to the exit, while in the configuration 7 it is located at the middle of that. In

Table 1
Location of the winglets of the investigated configurations

Configurations		x_{PA}	y_{PA}	x_{PB}	y_{PB}	x_{PC}	y_{PC}
3	First row	0.63	2.19	2.36	1.19	1.86	0.32
6	First row	0.63	2.19	2.36	1.19	1.86	0.32
	Second row	5.55	2.19	7.28	1.19	6.78	0.32
7	First row	0.63	2.19	2.36	1.19	1.86	0.32
	Second row	8.02	2.19	9.75	1.19	9.25	0.32
	First row	0.63	2.19	2.36	1.19	1.86	0.32
11	Second row	5.55	2.19	7.28	1.19	6.78	0.32
	Third row	10.47	2.19	12.2	1.19	11.7	0.32

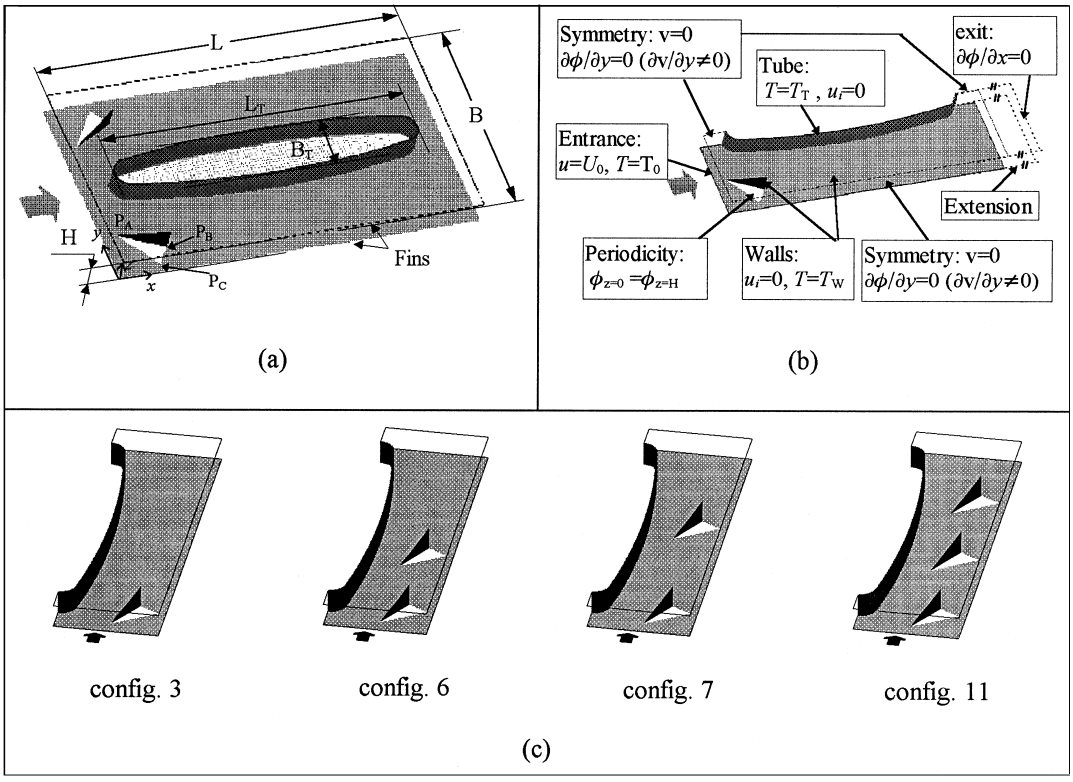

Fig. 3. (a) the geometrical model ($L = 15.4\ H$, $B = 9.1\ H$, $L_T = 12.8\ H$, $B_T = 2.34\ H$, $A_f/A_T = 8.44$); (b) the computational domain and the BCs; (c) the investigated configurations. In (a) and (b), only one DWP is exemplified since the same BCs are used for every winglet. The area ratio of each winglet to fin is 1.73%.

configuration 11, the second and the third DWP are located at 1/3 and 2/3 of the distance from the first winglet to the exit respectively. In the geometrical model and the computational domain in Fig. 3(a)–(b), just one DWP is exemplified because the same winglet and the same boundary conditions are used. On solid walls (tube, fin, winglet), no-slip conditions are used.

2.2. Mathematical model

The velocity and temperature fields in the channel were calculated by solving the unsteady three-dimensional Navier–Stokes and energy equations for an incompressible fluid with constant properties. The temperature field in the fin was obtained by solving the conduction equation. In dimensionless form these equations in curvilinear co-ordinate system with Cartesian velocity components and in index notation are,

$$\frac{\partial U_i}{\partial \xi_i} = 0 \tag{1}$$

$$J\frac{\partial u_k}{\partial t} + \frac{\partial}{\partial \xi_i}\left[U_i u_k - \frac{1}{Re}\frac{1}{J}\left(B^i_j\frac{\partial u_k}{\partial \xi_j} + \beta^i_j\omega^j_k\right) + p\beta^i_k\right] = 0 \tag{2}$$

$$J\frac{\partial T}{\partial t} + \frac{\partial}{\partial \xi_i}\left[U_i T - \frac{1}{Pe}\frac{1}{J}\left(B^i_j\frac{\partial T}{\partial \xi_j}\right)\right] = 0 \tag{3}$$

$$\frac{1}{Ft}J\frac{\partial T_f}{\partial t} - \frac{\partial}{\partial \xi_i}\left[\frac{1}{J}\left(B^i_j\frac{\partial T_f}{\partial \xi_j}\right)\right] = \frac{1}{Fi}J\dot{q} \tag{4}$$

with

$$U_i = u_j\beta^i_j, \quad B^i_j = \beta^i_k\beta^j_k, \quad \omega^i_j = \frac{\partial u_i}{\partial x_k}\beta^k_j$$

and

$$Re = \frac{u^*_0 H^*}{v^*_0}, \quad Pr = \frac{v^*_0}{a^*_0}, \quad Pe = Re\cdot Pr,$$

$$Fi = \frac{\delta^*}{H^*}\frac{k_f}{k^*_0}, \quad Ft = \frac{1}{Pe}\frac{a^*_f}{a^*_0}$$

where Einstein summation convention applies, and dissipation is neglected. β^i_j are the cofactors of $\partial x_i/\partial \xi_j$ in the Jacobian J of the coordinate transformation $x_i = x_i(\xi_j)$. Re, Pr, and Pe are the Reynolds number, the Prandtl number and the Peclet number. Assuming very small Biot number on the fin, the conduction in the fin can be considered two-dimensional. The conjugate heat transfer is further described by two parameters Fi and Ft.

In the equations (1)–(4), the time was non-dimensionalized by H^*/u^*_0, all lengths by H^*, the velocity components by the average velocity u^*_0. The temperature was the difference between the local and the inlet temperature scaled by the difference of the tube temperature and the inlet temperature. The pressure was the difference between the local and a reference pressure divided by $\rho^*_0 u^{*2}_0$. Variables with a subscript '0' refer to the state of the fluid at the entrance, with an 'f' to the fin, and with a 'T' to the tube. The dimensionless temperature at the inlet and on the tube is 0 and 1 respectively.

$\dot{q}$ stands for the convective heat removal on both sides of the fin. This term couples the convective heat transfer to the fins and conductive heat transfer in the fins. It can be expressed as:

$$\dot{q} = \dot{q}|_{z=0} - \dot{q}|_{z=1} \quad \text{with}$$

$$\dot{q}|_{z_0} = \frac{1}{J}\left(\frac{\partial T}{\partial \xi}\beta^1_3 + \frac{\partial T}{\partial \eta}\beta^2_3 + \frac{\partial T}{\partial \xi}\beta^3_3\right)_{z_0} \tag{5}$$

where $\dot{q}|_{z=0}$ and $\dot{q}|_{z=1}$ denote the heat removal on the lower and upper side of the fin. They were non-dimensionalized by dividing $(T^*_T - T^*_0)k^*_0/H^*$.

2.3. Numerical solution

A grid generation technique by solving the Poisson equation [11] was used to discretize the computational domain into a finite number of control volumes. The differential equations (1)–(4) were discretized by a finite-volume method [12]. The convective terms were discretized with a 'flux blending' scheme, in which the convective flux was split into an upwind difference (UD) and a central difference (CD), and treated with a 'deferred-correction approach' [13], in which the UD part was calculated implicitly, while the difference between the CD and UD part was calculated explicitly. SIMPLEC algorithm [14] were used for pressure-velocity correction. To avoid decoupling of the velocity and pressure field caused by the co-located arrangement of the dependent variables, a momentum interpolation was applied [15]. The algebraic equation system was solved by a strongly implicit procedure (SIP) of Stone [16], in which the original coefficient matrix was incompletely split to a product of a lower and an upper matrix and solved iteratively. More descriptions of the solution procedure can be found in [17–19]. The numerical solution of the velocities and temperature fields for one time step was carried out with the following procedure:

(1) The momentum equations were solved with best available initial values.
(2) A pressure-velocity correction based on SIMPLEC was performed.
(3) Steps 1 and 2 were repeated until a divergence-free velocity field was obtained.
(4) The energy equation was solved with the known velocity field and the updated temperature field on the fin and in the fluid.
(5) The local heat flux to the fin $\dot{q}(x, y)$ was calculated.
(6) The heat conduction equation was solved with the local heat flux as heat sources.
(7) Steps 4–6 were repeated until a converged solution was obtained. The convergence criterion is 10^{-5}.

2.4. Validation of the procedure

The fundamental program code was verified for complex oscillating flow in ducts with vortex generator [20] and flows in hydrodynamical couplings [19].

The program code and the basis configuration used in this study were the same as those in the earlier investigations [4, 5, 21, 22, 23]. Computations were performed on an IBM-RISC-System/6000/530H on curvilinear grids of 152*60*24 points along x, y and z coordinates. A divergence-free criterion of 10^{-5} was prescribed. For an FOT with $Re = 300$ and $Fi = 500$, the grid convergence index [24] is 1.338% for the apparent friction number f and 3.51% for the Colburn j factor [18]. Numerical–experimental comparisons of the Nusselt number distribution in the FOT showed perfect agreement of the measured [25] and computed results [5, 22, 23].

3. Results and discussions

In compact heat exchangers, a very important range of Reynolds number lies under 500 [26]. In this study, Reynolds numbers $Re = 300$ and the fin parameter Fi of 100, 500, 1000, and ∞ are used with air ($Pr = 0.7$) as fluid. From the computed temperature and pressure field, local heat flux $\dot{q}$, Nusselt number Nu, apparent friction number f_{app} etc were calculated. The heat flux on both sides of the fin $\dot{q}$ is defined in equation 5. The local Nusselt number is defined with the local heat flux, the local fin temperature and the bulk temperature of the respective cross section:

$$Nu(x,y)|_{Z=0} = \frac{\dot{q}(x,y)|_{z=0} D}{T_f(x,y) - T_B(x)} \tag{6}$$

where D is the dimensionless characteristic length. D is one when the same characteristic length H as in the definition of Re is used. The bulk temperature is defined as,

$$T_B(x) = \frac{\iint |u(x,y,z)| T(x,y,z)\,\mathrm{d}y\,\mathrm{d}z}{\iint |u(x,y,z)|\,\mathrm{d}y\,\mathrm{d}z}. \tag{7}$$

The spanwise averaged Nusselt number $Nu_{sp}(x)$ and heat flux $\dot{q}_{sp}(x)$ are defined as,

$$Nu_{sp}(x) = \frac{1}{B_{fl}(x)} \int_0^{B_{fl}(x)} Nu(x,y)\,\mathrm{d}y \tag{8}$$

and

$$\dot{q}_{sp}(x) = \frac{1}{B_{fl}(x)} \int_0^{B_{fl}(x)} \dot{q}(x,y)\,\mathrm{d}y \tag{9}$$

where $B_{fl}(x)$ refers to the wetted width of the duct in that y-z-plane. The cross sectional average pressure $p_{cs}(x)$ is defined as,

$$p_{cs}(x) = \frac{\iint p(x,y,z)\,\mathrm{d}y\,\mathrm{d}z}{\iint \mathrm{d}y\,\mathrm{d}z}. \tag{10}$$

3.1. Flow patterns

For in-line winglets, 'new' LVs with the same circulating direction were generated by the winglets downstream. Figure 4 shows velocity vectors (Fig. 4(a)–(c)) and streamlines (Fig. 4(d)–(f)) of the secondary flow in eight cross-sections in configurations 6, 7 and 11 for $Re = 300$. Immediately behind the second winglet, two closely located vortical flow systems can be observed. The bigger and stronger one to the tube side is generated by the second winglet and the smaller one to the lateral side comes from the first winglet (see the fourth section in Fig. 4(a) (c) (d) and (f) and the fifth section in Fig. 4(b) and (e)). The two co-rotating vortices soon coalesce and form a bigger one. So the vortices behind the secondary winglet are stronger than those behind the first one. And for configuration 11, the LVs behind the third winglet are stronger than those behind the second winglet. For configuration 11, the core of the vortices upstream and downstream of the third winglet seem to overlap (Fig. 4(c) section 6), and the LVs are much stronger than those downstream of the second winglet, as shown in Fig. 4(g–i). Figure 5 shows pressure distributions in the x-y-plane of $z = 0.5$ of configurations 6 and 7 at $Re = 300$. The regions with pressure minimum behind the winglets correspond to the vortex cores. Behind the first winglet, pressure difference between the LV-core and their surroundings is smaller than that behind the second winglet. Due to the existence of two cores immediately behind the second winglet, the area of pressure minimum is bigger than that behind the first winglet.

To study the interaction of the 'old' and the 'new' LVs, we first consider the streamlines (SLs) on the cores of the LVs (Fig. 6). In Fig. 6(a), the SLs on the LV-cores generated by the first and the second winglet for configuration 6 are combined. In Fig. 6(b), only the SLs on the LV-core by the first winglet in the configuration 11 are shown. Comparing Fig. 6(a) and (b), we notice that the coming LV-core of the first winglet pass around the trailing edge of the second winglet, keeps its identity for a short distance, and then merge into the body of the new LV. They wrap the SLs of the second LV-core farther downstream. In Fig. 6(b), the SLs of the first LV-core join the second LV-body first, then pass partly over the leading edge and partly around the trailing edge of the third winglet, diverge once more, burst, and finally join in the outer layer of the LVs by the third winglet. In Fig. 6(c), the SLs of the LV-core by the second winglet stem predominantly from the fluid outside the coming LVs generated by the first winglet, and they diverge as they pass the third winglet. These cannot be seen clearly on

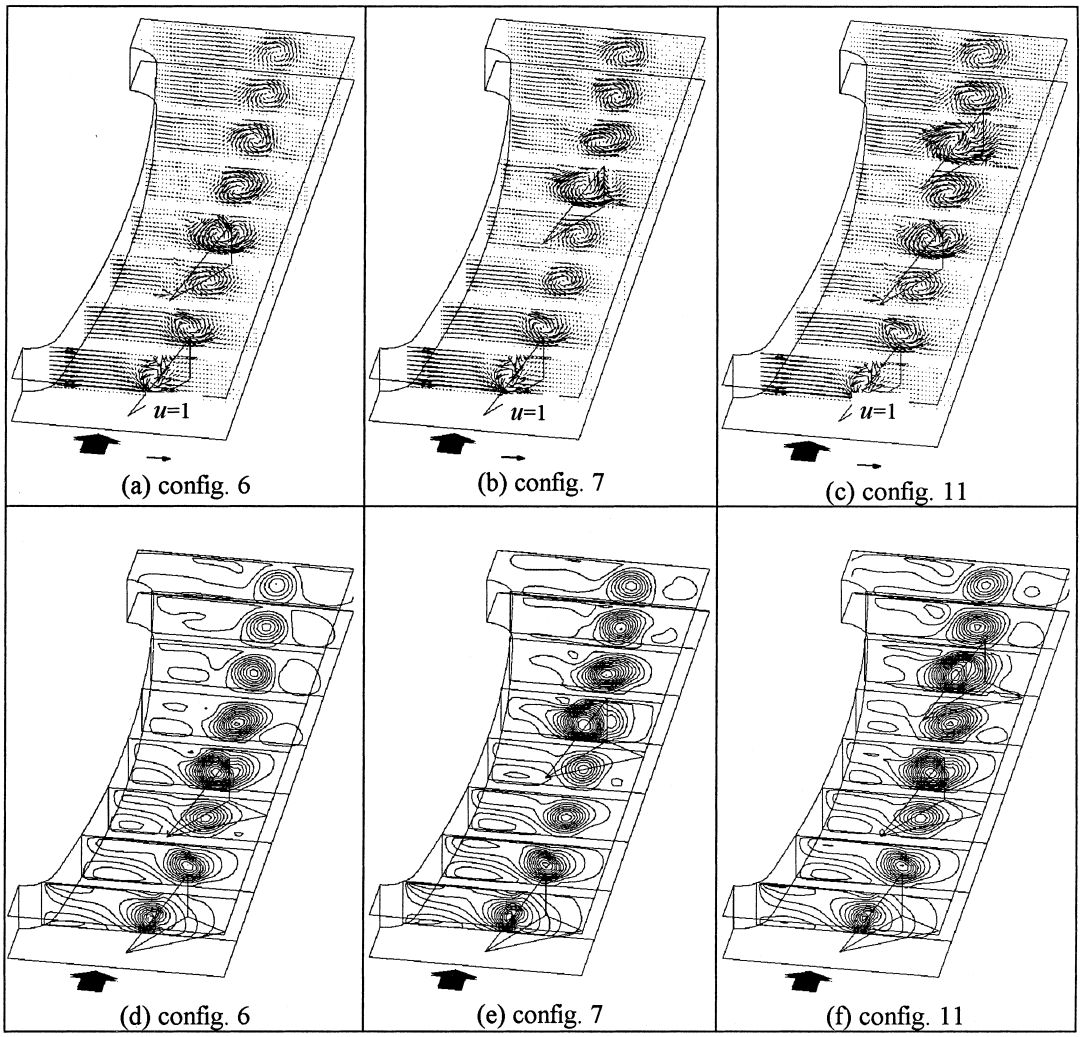

Fig. 4. (a)–(c) Vector plots of the secondary flow in eight cross sections in the streamwise direction for $Re = 300$. The eight sections are at $x = 1.5$, 3.5, 5.6, 7.7, 9.7, 11.8, 13.8 and 15.4 respectively; (d)–(f) the corresponding streamlines of the secondary flow; (g)–(i) enlargement of the second, fourth, and sixth section in Fig. 4(c) showing the stepwise increasing magnitude of the secondary flow velocities and the increasing size of the vortices behind the first, second and third winglet for configuration 11.

the vector-plots in Fig. 4. The SLs of the third LV-core, which are wrapped by the SLs of the second LV-core, stem from the outer layer of the coming LVs (Fig. 6(d)).

The LVs result first of all from the flow separation on the leading edge of the winglet. Figure 7(a)–(b) show the SLs form the leading edge of the first winglet and their projection in the y–z-plane in configuration 6 for $Re = 300$. These SLs constitute the core and its neighborhood of the LV. Except for two SLs from the corner of the leading and trailing edge which run outside the primary LV, almost all of the SLs pass the second winglet around the trailing edge, which can be seen clearly in the projection of SLs in the y–z-plane (Fig. 7(b)). In Fig. 7(c), the SLs from the fluid on the leading edge of the second winglet form the core and its vicinity of the second LV. There are also two SLs from the corner of the leading and trailing edge running outside the core and join in the outer layer of the LV. In the wake of the second winglet, the SLs from the leading edge of the first winglet wrap around those from the second winglet. Figure 8 shows the SLs from the leading edge of the winglets in configuration 11 with $Re = 300$. They pass the second winglet around the trailing edge (Fig. 8(a), (b)), diverge, and join the body of the LVs generated by the second winglet. After passing the third winglet, most of them diverge once more, burst and run outside the LV. The SLs from the second winglet pass the third winglet partly over the leading edge and partly around the trailing edge

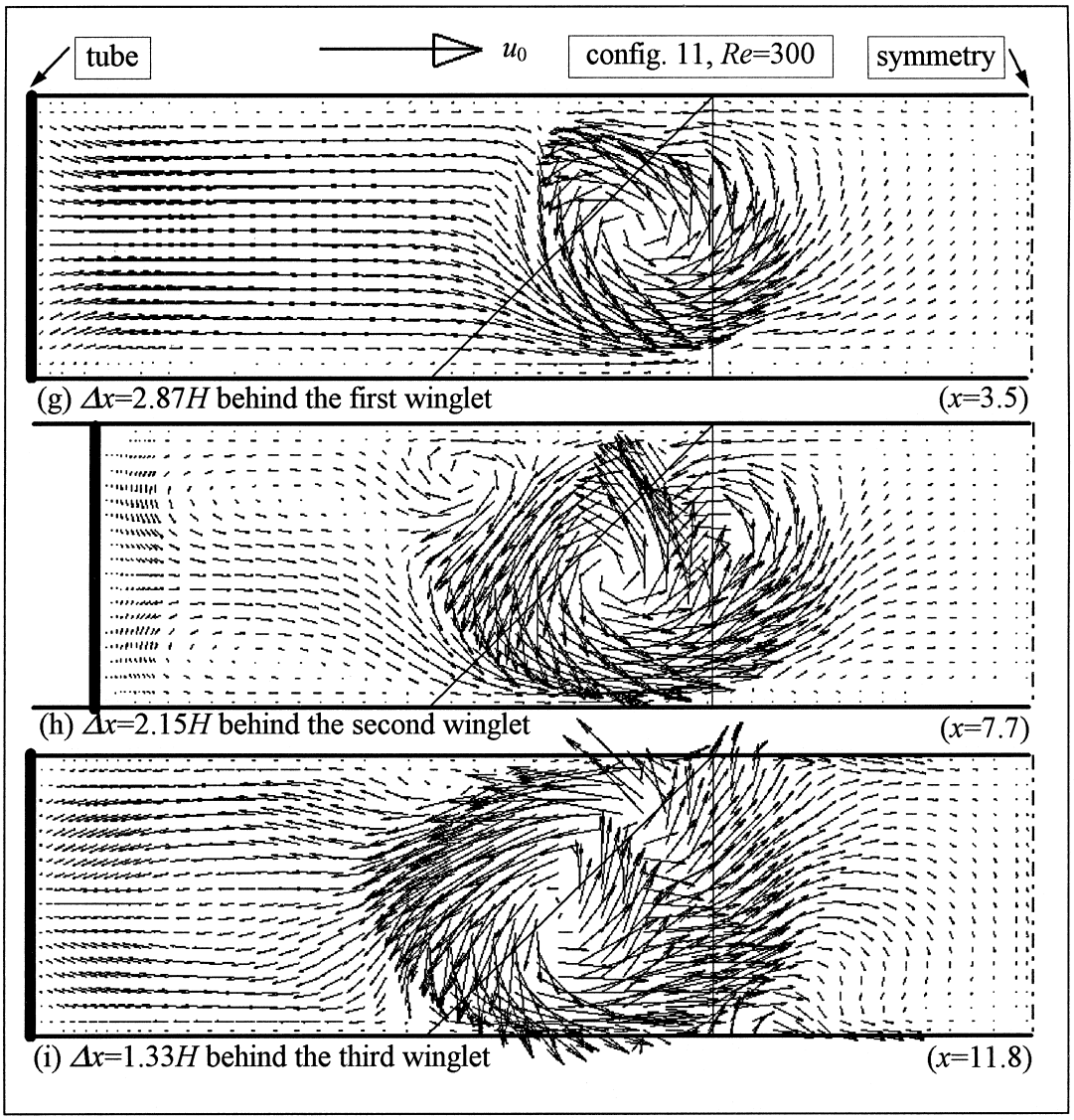

Fig. 4—*continued.*

(Fig. 8(d), (e)). They diverge after passing the third winglet and swirl down the stream. If the SLs from the three winglets are combined (Fig. 8(f)), a more complex LV system appears.

3.2. Heat transfer

The fin temperatures are changed by the punching of the winglets. Figure 9 compares the fin temperatures of the configurations 6 and 7 with $Re = 300$ and $Fi = 500$. The fin temperature distribution shows two low temperature regions, one around the first winglet near the leading edge of the fin, the other in the middle of the fin around the second winglet. In the range of $4 < x < 8$, the fin temperatures near the lateral boundary for configuration 6 are smaller than those for configuration 7. This is contrary to that at $x > 9$. The fluid temperature distributions are disturbed by the swirling flow as shown in Fig. 10, where the temperature distributions on eight sections of configurations 6 and 11 with $Re = 300$ and $Fi = 500$ are compared. There are two thermal boundary layers, one on the fin, and the other on the tube. In the effect region of the LVs, the isotherms are stretched. The 'down-wash' and 'up-wash' of the LVs on both sides and both channel walls can be observed by the thinned and thickened thermal boundary layers. From section (a) to

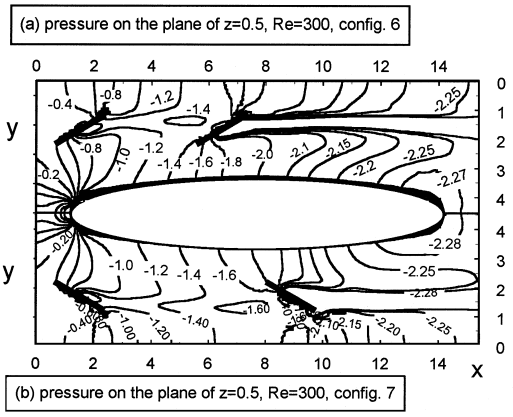

Fig. 5. Dimensionless pressure $p(x, y, z)$ on the x–y-plane of $z = 0.5$ in configurations 6 and 7 at $Re = 300$.

(e), the temperature distributions of configurations 6 and 11 are nearly the same. Beginning with section (f), the isotherms of configuration 11 are further stretched.

Figure 11 shows the fin heat fluxes and Fig. 12 the fin Nusselt numbers for configurations 6 and 7 with $Re = 300$ and $Fi = 500$. From $x = 0$ to $x \approx 5$ and in the tube wake, the heat fluxes are nearly the same for the two configurations. The distributions of $\dot{q}$ and Nu show two developing regions behind the winglets, where the isolines show a higher peak and two lower ones. The higher peak results from the primary LVs and the lower ones form the induced and corner vortices [28]. In the vicinity of the tube, the heat fluxes and Nusselt number in both configurations are the same because they have not been influenced by the LVs.

For the FOT without winglet (configuration 0), the fin parameter Fi in the range of 100 and 1000 does not have a significant influence on the fin heat transfer [21–23]. For the FOT with winglets, the influence of Fi depends on the number of winglets punched from the fin. Figure 13 shows the dependence of the span-averaged heat fluxes on Fi for configuration 6 at $Re = 300$. The largest difference in $\dot{q}_{sp}$ with respect to Fi occurs in the proximity of the winglets, where the local maximum heat transfer occurs and the local minimum fin temperature appears. In the rear part of the fin, the differences vanish.

Figure 14(a) shows the span-averaged Nusselt number enhancement $R_{Nu} = Nu_{sp}(x)/Nu_{0,sp}(x)$ in configurations 6 and 7 with respect to that in configuration 0 ($Nu_{0,sp}(x)$). Upstream of the first winglet, R_{Nu} is a little less than one due to the lowered fin temperatures at the leading edge of the fin by the punched winglet. Upstream of the second winglet in configuration 6, the two curves are identical. between the first and the second winglet, R_{Nu} increases extremely slowly. The peak of R_{Nu} by the second winglet is higher than that by the first one, and the peak by the second winglet of configuration 7 is higher than that of configuration 6; and so are those downstream of the second winglet. These indicate that the local R_{Nu} by a winglet downstream is higher than that by a winglet upstream. It seems that configuration 7 is better than configuration 6 in HTE. But the HTE by the second winglet in configuration 6 takes place earlier. And the difference between the two curves at $x \approx 6.8$, where the peak value of configuration 6 appears, is larger than that at $x \approx 9.3$, where the peak value in configuration 7 occurs. So the global Nusselt number enhancement ($R_{Nu} = 1.3$) is surprisingly the same for configurations 6 and 7. In Fig. 14(b), R_{Nu} for configurations 3, 6 and 11 are presented. R_{Nu} is stepwise increased by each winglet. Upstream of the second winglet, the three curves merge to one. Upstream of the third winglet in configuration 11, the curves for configurations 6 and 11 are almost the same. The difference of the peak values between the first and the second winglet is larger than that between the second and the third winglet. The global R_{Nu} is 1.15, 1.3 and 1.4 for configurations 3, 6 and 11 respectively (for $Re = 300$, $Fi = 500$). So the first and the second winglets provide the same heat transfer enhancement, while the third winglet in configuration 11 shows only 66.7% that of the heat transfer enhancement by the first or the second winglet.

The HTE is accompanied by extra pressure losses. Figure 15(a) compares the spanwise averaged pressure distribution in configurations 0, 6 and 7 with $Re = 300$. Comparing these curves, we can identify the form drag of the tube. Immediately behind the winglets, a small increase in pressure can be observed, which results from a sudden expansion of the flow passage. The biggest pressure difference between configurations 6 and 7 occurs in the range from $x \approx 6$ to $x \approx 10$. The difference disappears at the exit. Figure 15(b) compares the pressure distribution in configurations 0, 3, 6, and 11. We can see a stepwise reduction of the pressure. The pressure drop caused by the first winglet is smaller than that by the third winglet, which in its turn is smaller than that caused by the second winglet. The quasi-parallel curves in Fig. 15(b) confirm the deduction of Fiebig et al. [29] from the measured global drag values that the form drag of the LVGs is predominant for the pressure drop, and the LVs themselves hardly cause any additional pressure drop of the flow.

The thermohydraulic performance factor $R_p = (j/j_0)/(f/f_0)$ is 1.04, 1.01, 1.00 and 0.97 for configurations 3, 6, 7, and 11 respectively at $Re = 300$ and $Fi = 500$.

4. Concluding remarks

Flow pattern analysis shows:

- The form drag of the winglets is responsible for the

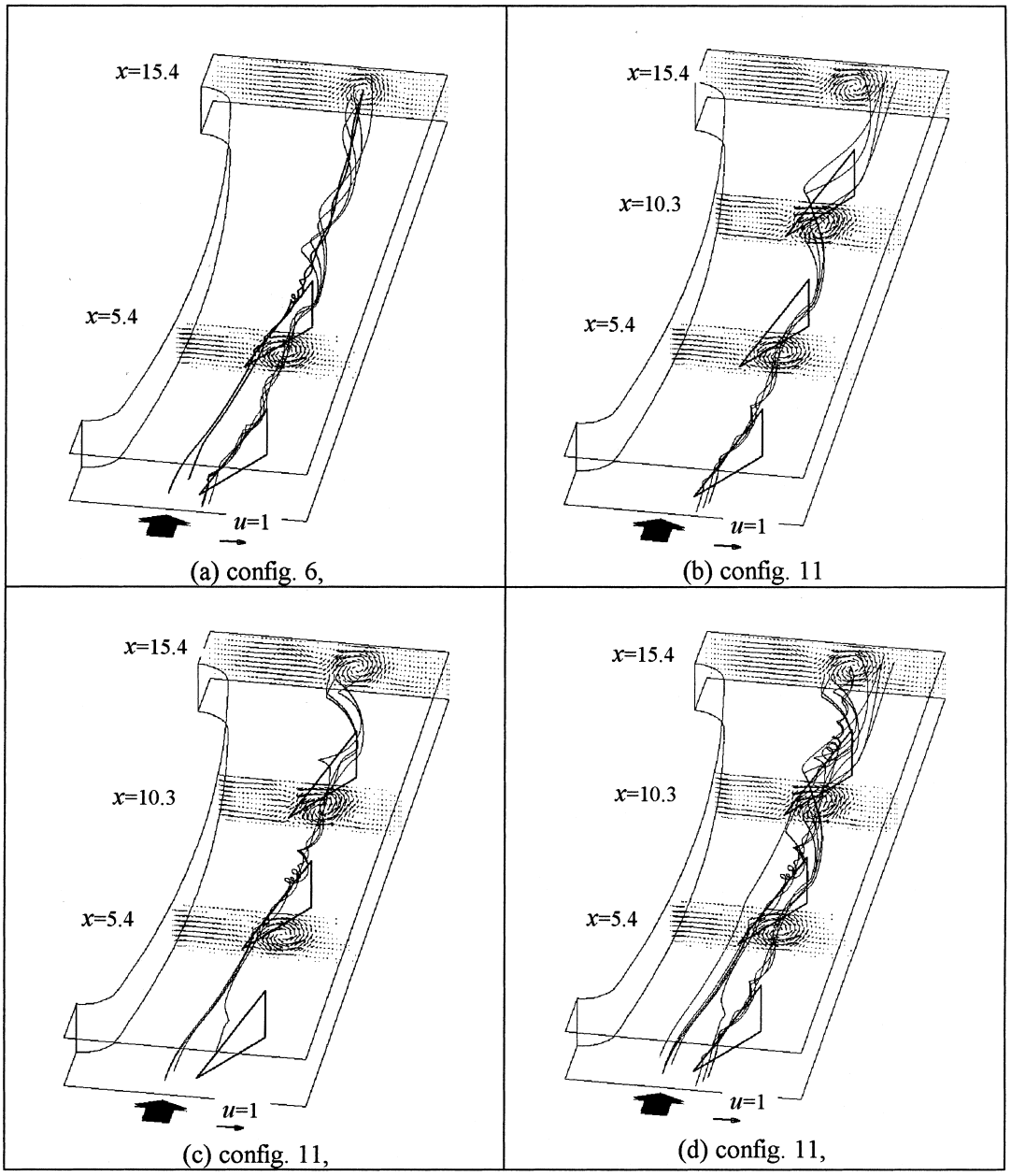

Fig. 6. Selected streamlines (SLs) along the LV-cores at $Re = 300$; (a) SLs for the first and second winglet of configuration 6; (b)–(c) SLs for the first and second winglet of configuration 11; (d) combination of the SLs for the first, second, and third winglet of configuration 11.

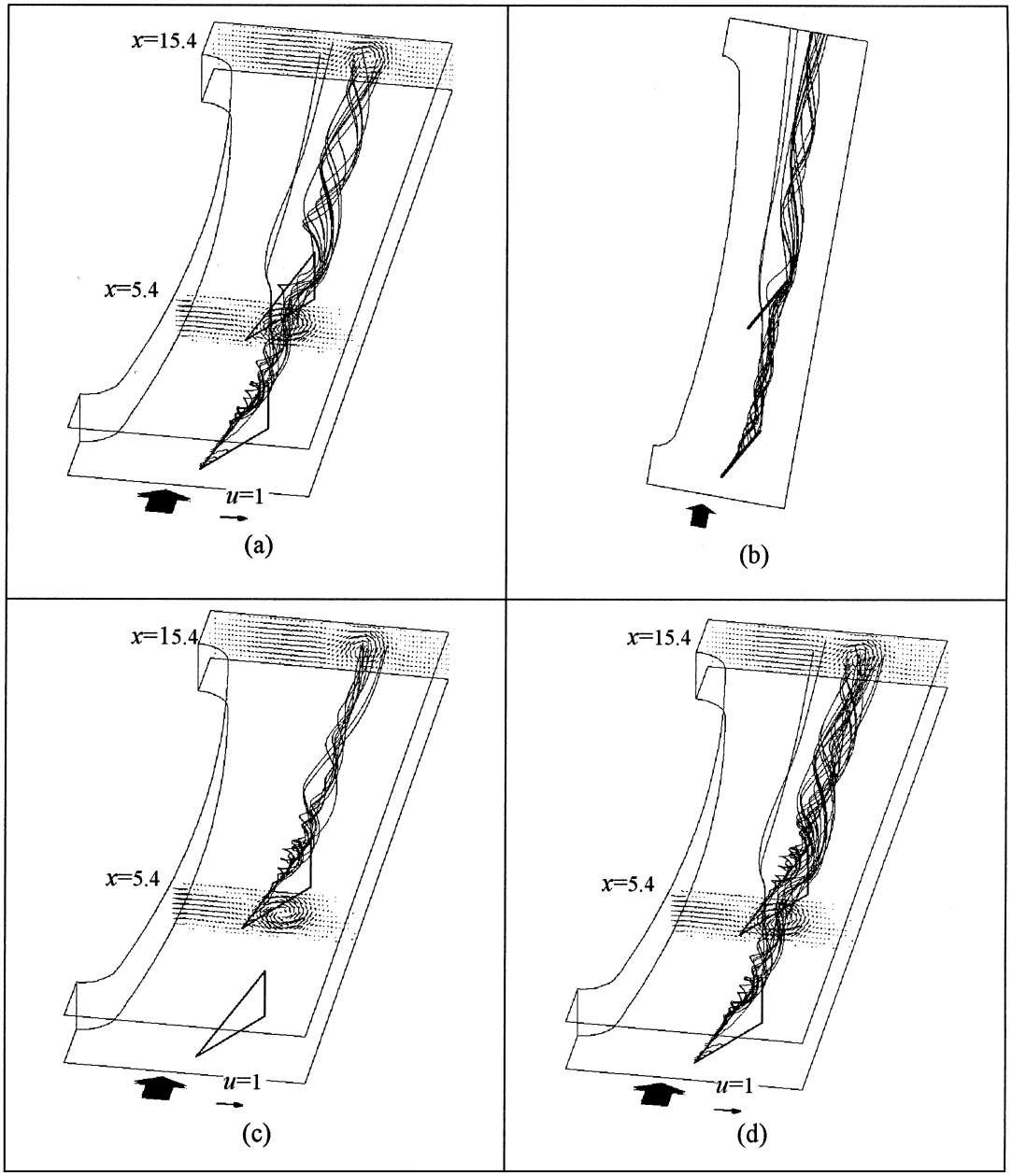

Fig. 7. SLs from the leading edges of the two winglets in configuration 6 ($Re = 300$); (a)–(b) SLs from the fluid on the leading edge of the first winglet and their projection; (c) SLs from the fluid on the leading edge of the second winglet; (d) combination of (a) and (c).

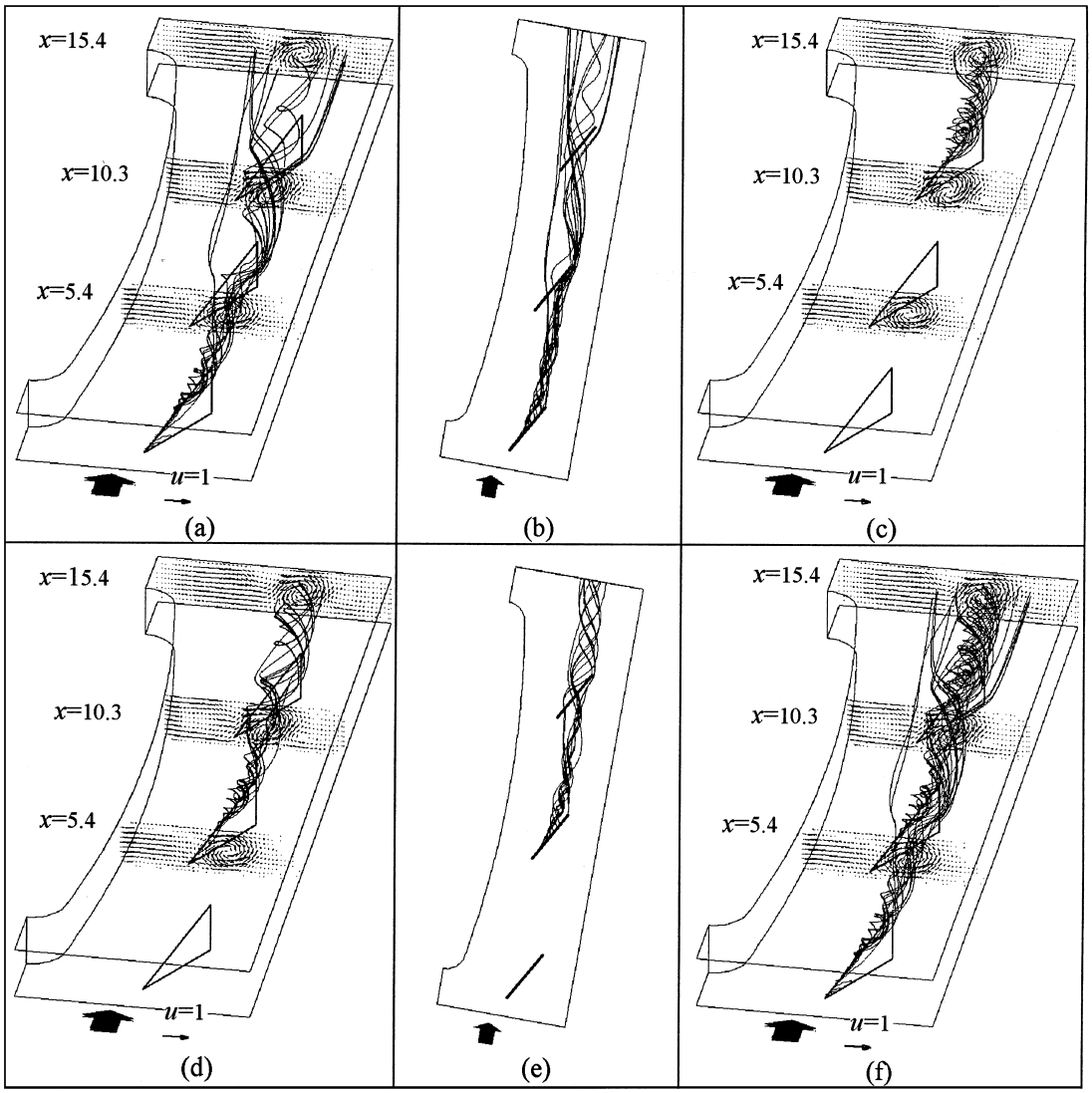

Fig. 8. SLs from the leading edges of the winglets in the configuration 11 (Re = 300); (a)–(b) SLs from the leading edge of the first winglet and their projection on the x-y-plane. (c) SLs from the leading edge of the third winglet; (d)–(e) SLs from the leading edge of the second winglet and their projection on the x–y-plane; (f) combination of (a), (c) and (d).

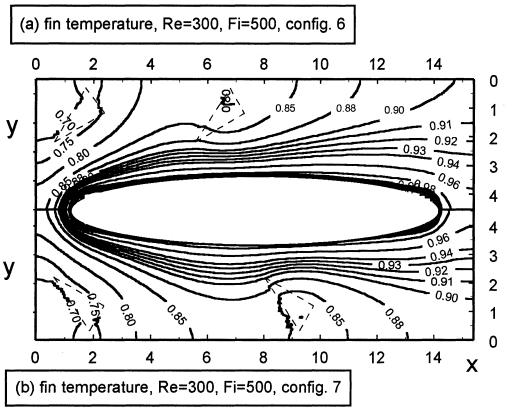

Fig. 9. Dimensionless fin temperatures $T_f(x, y)$ in configurations 6 and 7 at $Re = 300$ and $Fi = 500$.

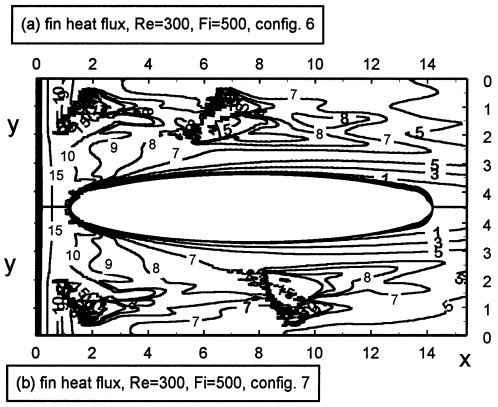

Fig. 11. Comparison of the dimensionless fin heat fluxes in configurations 6 and 7 at $Re = 300$ and $Fi = 500$.

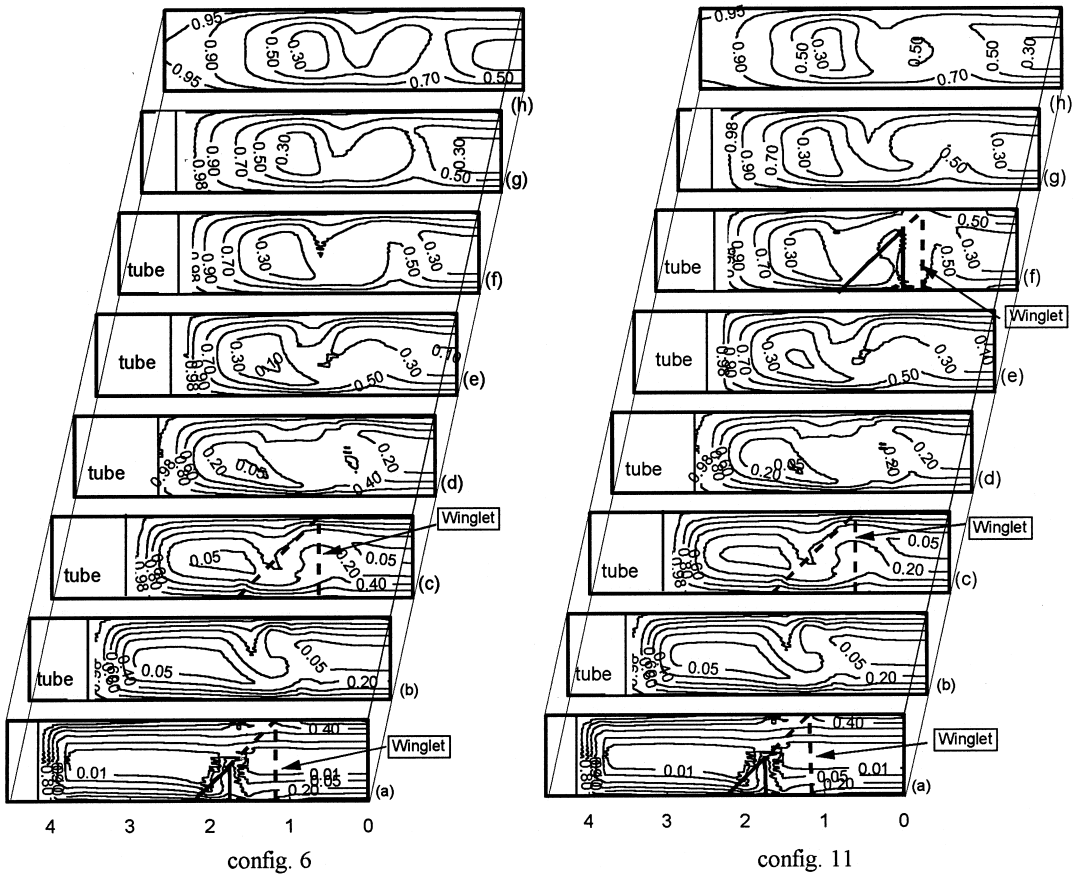

Fig. 10. Dimensionless fin temperatures $T(x, y, z)$ in eight sections of configurations 6 and 11 for $Re = 300$ and $Fi = 500$. From (a) to (h), x is located at 1.5, 3.5, 5.6, 7.7, 9.7, 11.8, 13.8 and 15.4, respectively. Solid or dashed lines show that winglet parts are upstream or downstream of the sections where winglets are drawn, respectively.

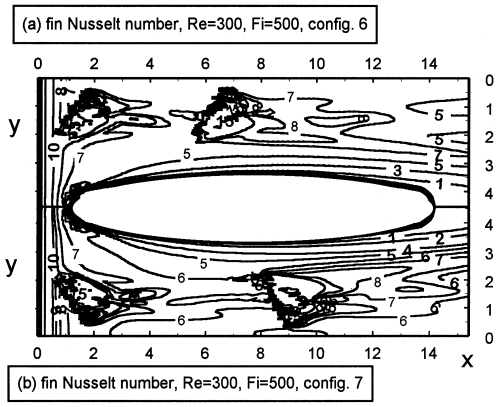

Fig. 12. Comparison of the fin Nusselt numbers in configurations 6 and 7 at $Re = 300$ and $Fi = 500$.

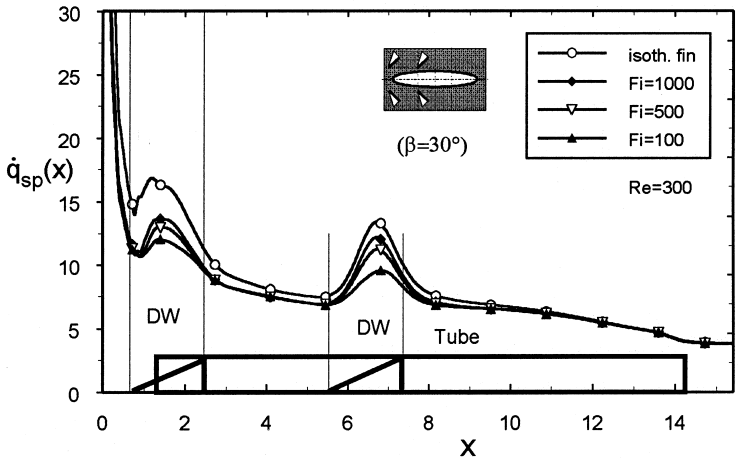

Fig. 13. Dependence of the span-averaged fin heat fluxes in configuration 6 on the fin parameter *Fi*.

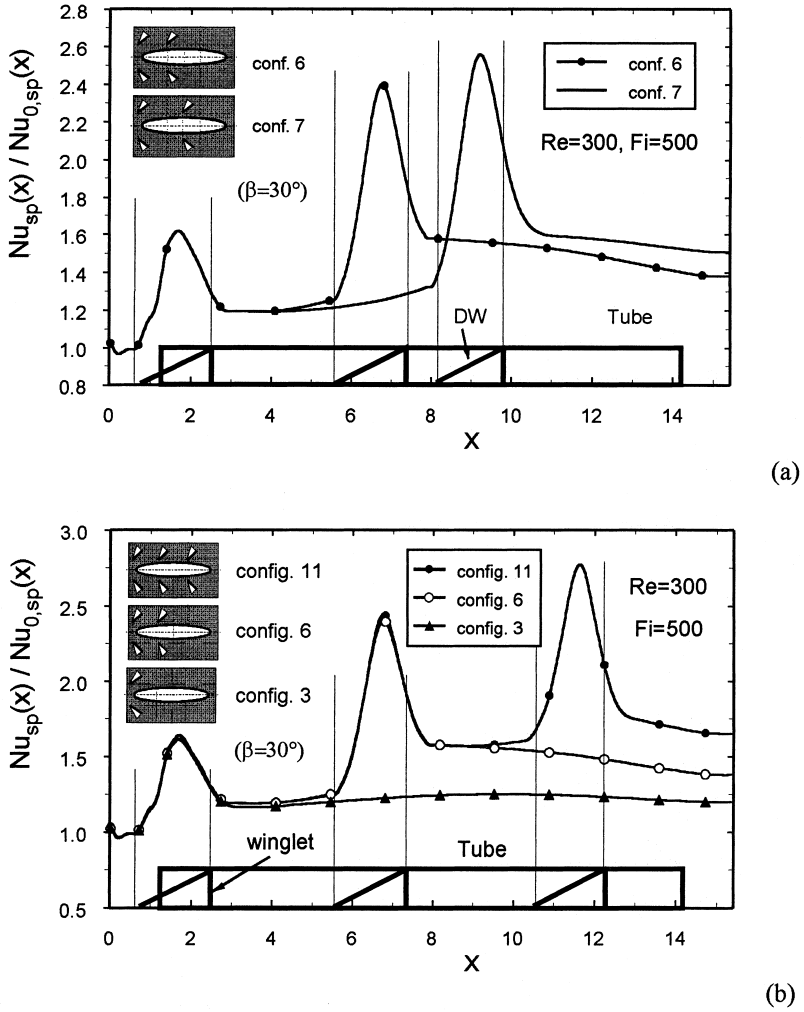

Fig. 14. Comparison of the Nusselt number enhancements in configurations 6 and 7(a) and in configurations 3, 6 and 11(b). Nu_0 is the Nusselt number in an FOT without winglet (configuration 0).

pressure drop, which depends strongly on the local streamwise velocity.

- Immediately behind the second winglet, two vortical flow systems exist. The one from the winglet upstream keeps its identity for a short distance and then merges into the new LVs generated by the second winglet.
- If streamlines of the LVs, either from the LV-core or the LV-body, collide on a winglet downstream, they diverge.
- The stronger LVs behind the second and the third winglet results from the superimposition of the coming LVs and the newly generated LVs.

Analysis of the temperature field and heat transfer distribution shows:

- The temperature distribution in the flow passage is stretched by the LVs.
- *Fi* influences the heat fluxes in the neighborhood of the winglets strongly, but hardly those in the rear part of the fin.
- In developing flow, local Nusselt number enhancement R_{Nu} caused by a winglet downstream is higher than a winglet upstream, global R_{Nu} is just the opposite of that.

A winglet in the rear part of the fin such as the third one

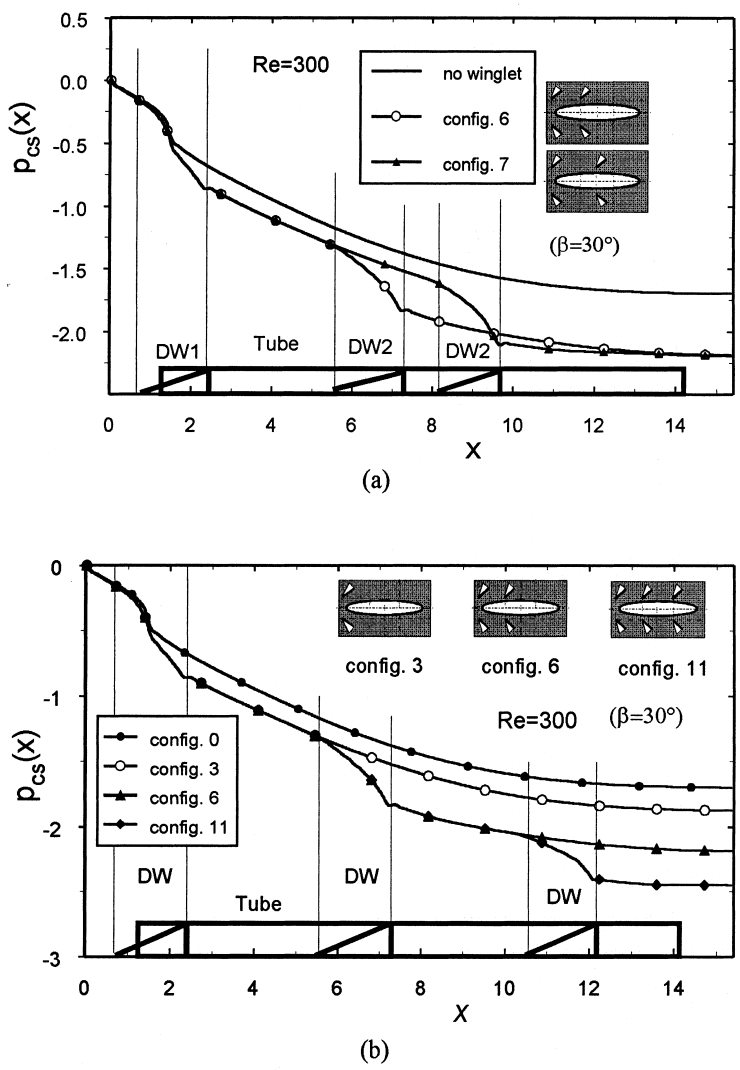

Fig. 15. Comparison of the cross-sectional averaged pressure $p_{cs}(x)$ in (a) configuration 6 and 7 and in (b) configurations 3, 6 and 11.

in configuration 11 enhances only 66.7% of the heat transfer enhancement by the first or by the second winglet, but causes a pressure drop larger than that by the first winglet. The thermohydraulic performance of configuration 11 is poorer than that of configuration 6. The performance of configuration 6 is also slightly superior to that of configuration 7.

References

[1] M. Fiebig, Vortex generators for compact heat exchangers, Int. J. of Enhanced Heat Transfer 2 (1–2) (1995) 43–61.
[2] M. Fiebig, Embedded vortices in internal flow: Heat transfer and pressure loss enhancement, Int. J. of Heat and Fluid Flow 16 (5) (1995) 376–388.
[3] M. Fiebig, Vortices and heat transfer, ZAMM, Z. angew. Math. Mech 77 (1) (1997) 3–18.
[4] Y. Chen, M. Fiebig, N.K. Mitra, Influence of the angle of attack of a wing-type VG on the heat transfer and flow loss of a finned oval tube, Proceedings of the Eurotherm Seminar 55, Heat Transfer in Single Phase Flows 5, Santorin, Greece, September, 1997.
[5] Y. Chen, M. Fiebig, N.K. Mitra, Conjugate heat transfer of a finned oval tube with a punched longitudinal vortex generator in form of a delta winglet—parametric investigations of the winglet, Int. J. Heat Mass Transfer 41 (23) (1998) 3961–3978.
[6] S. Tiggelbeck, Experimentelle Untersuchungen an Kan-

alströmungen mit Einzel- und Doppelwirbelerzeuger-Reihen für den Einsatz in kompakten Wärmetauschern, dissertation, Institute für Thermo- und Fluiddynamik, Ruhr-Universität Bochum, 1990.

[7] T. Güntermann, Dreidimensionale stationäre und selbsterregt-schwingende Strömungs- und Temperaturfelder in Hochleistungswärmeübertragern mit Wirbelerzeugern, dissertation, Institut für Thermo- und Fluiddynamik, Ruhr-Universität Bochum, 1992.

[8] A. Bastani, Numerische Untersuchung von Wärmeübergang und Strömungsverlust in Lamellen-Rohr-Wärmeübertragern mit Längswirbelerzeugern, dissertation, Institut für Thermo- und Fluiddynamik, Ruhr-Universität Bochum, 1992.

[9] A. Valencia, Wärmeübergang und Druckverlust in Lamellen-Rohr-Wärmeüberragern mit Längswirbelerzeugern, dissertation, Institut für Thermo- und Fluiddynamik, Ruhr-Universität Bochum, 1993.

[10] W.M. Kays, A.L. London, Compact Heat Exchangers, 3rd ed. McGraw-Hill Book Company, New York, 1984.

[11] A. Hilgenstock, A fast method for elliptic generation of 3D grids with full boundary control, in: S. Sengupta et al. (Eds.), Numerical Grid Generation in Computational Fluid Mechanics, Swansea, Pineridge, 1988, pp. 137–146.

[12] S.V. Patankar, Numerical Heat Transfer and Fluid Flow, Hemisphere Publishing Corporation, 1980.

[13] P.K. Khosla, S.G. Rubin, A diagonally dominant second-order accurate implicit scheme, Comp. Fluid 2 (1974) 207–209 s.

[14] J.P. Van Doormaal, G.D. Raithby, Enhancements of the SIMPLE method for predicting incompressible fluid flows, Numerical Heat Transfer 7 (1984) 147–163.

[15] C.M. Rhie, W.L. Chow, Numerical study of turbulent flow past an airfoil with trailing edge separation, AIAA J. 21 (11) (1983) 1525–1532.

[16] H.L. Stone, Iterative solution of implicit approximations of multidimensional partial differential equations, SIAM J. Numer. Anal. 5 (3) (1968) 530–558.

[17] M.A. Peric, Finite volume method for the prediction of three-dimensional fluid flow in complex ducts, Ph.D. thesis, University of London, 1985.

[18] Y. Chen, Leistungssteigerung von Wärmeübertragern mit berippten Ovalrohren durch Längswirbelerzeugern—Numerische Simulation von Strömung und konjugiertem Wärmeübergang, dissertation, Institut für Thermo- und Fluiddynamik, Ruhr-Universität Bochum, 1997.

[19] A. Kost, Strömungsstruktur und Drehmomentübertragung in hydrodynamischen Kupplungen, dissertation, Institut für Thermo- und Fluiddynamik, Ruhr-Universität Bochum, 1993.

[20] A. Große-Gorgemann, Numerische Untersuchung der laminaren oszillierenden Strömung und des Wärmeübergangs in Kanälen mit rippenförmigen Einbauten, dissertation, Institut für Thermo- und Fluiddynamik, Ruhr-Universität Bochum, 1995.

[21] Y. Chen, M. Fiebig, N.K. Mitra, Numerical investigation of fin efficiencies in a finned oval tube, Proceedings of the 15th IMACS World Congress, vol. 5, Berlin, 24–29 August 1997, pp. 661–666.

[22] Y. Chen, M. Fiebig, N.K. Mitra, Conjugate heat transfer of a finned oval tube, Part A: flow patterns, Numerical Heat Transfer, Part A, 33 (1998) 371–385.

[23] Y. Chen, M. Fiebig, N.K. Mitra, Conjugate heat transfer of a finned oval tube, Part B: Heat transfer behaviors, Numerical Heat Transfer, Part A, 33 (1998) 387–401.

[24] P.J. Roache, A Method for uniform reporting of grid refinement studies, in Quantification of Uncertainty in Computational Fluid Dynamics, ASME FED-Vol. 158, 1993, pp. 109–120.

[25] R.K. Shah, M.S. Bhatti, Laminar convective heat transfer, in: S. Kakaç, R.K. Shah, W. Aung (Eds.), Handbook of Single-Phase Convective Heat Transfer, John Wiley and Sons, 1987.

[26] A.M. Jacobi, R.K. Shah, Heat transfer surface enhancement through the use of longitudinal vortices: a review of recent progress, Exp. Therm. Fl. Sci. 11 (1995) 295–309.

[27] W.R. Pauley, J.K. Eaton, Experimental study of the development of longitudinal vortex pairs embedded in a turbulent boundary layer, AIAA Journal 26 (7) (1988) 816–823.

[28] G. Biswas, K. Torii, D. Fujii, K. Nishino, Numerical and experimental determination of flow structure and heat transfer effects of longitudinal vortices in a channel flow, Int. J. Heat Mass Transfer 39 (16) (1996) 3441–3451.

[29] M. Fiebig, P. Kalweit, N.K. Mitra, Wing type vortex generators for heat transfer enhancement, Proceedings of the Eighth IHTC, vol 6, 1986, pp. 2909–2913.